CrystEngComm

PAPER

View Article Online
View Journal | View Issue

Cite this: *CrystEngComm*, 2025, **27**, 7063

Efficient capture of Sr^{2+} ions by a layered crystalline zirconium phosphate fluoride

Ziyuan Chen,[abc] Shuzhen Liu,[bc] Shuangjiang Li,[bc] Zhihua Chen,[bc] Lu Yang,[bc] Shengmao Zhang,[a] Haiyan Sun, *[bc] Meiling Feng *[bc] and Xiaoying Huang [bc]

The effective remediation of radioactive strontium-90 (^{90}Sr) from complex aqueous environments remains challenging due to the inherent high solubility and migration propensity of Sr^{2+} ions. Herein, we synthesized hydrothermally a new two-dimensional (2D) crystalline zirconium phosphate fluoride $[(CH_3)_2NH_2][Zr(PO_4)F_2]$ featuring a layered anionic architecture of $[Zr(PO_4)F_2]_n^{n-}$ with intercalated $[(CH_3)_2NH_2]^+$ cations, which shows exceptional Sr^{2+} remediation capability. It possesses a high maximum Sr^{2+} adsorption capacity (q_m^{Sr}) of 161.48 mg g^{-1} (higher than that of many inorganic crystalline adsorbents) and fast kinetics for Sr^{2+} capture (Sr^{2+} removal rate (R^{Sr}) of 94.89% within 1 min). Specifically, it maintains Sr^{2+} removal efficiency in the presence of competing Cs^+, K^+, Na^+, Ca^{2+}, Mg^{2+} ions and in actual aqueous systems including seawater (R^{Sr} = 79.06%). X-ray photoelectron spectroscopy (XPS) and thermodynamics confirm that spontaneous Sr^{2+} capture occurs through ion exchange processes, where the interlayered $[(CH_3)_2NH_2]^+$ cations in $[(CH_3)_2NH_2][Zr(PO_4)F_2]$ are exchanged with Sr^{2+}. The compound $[(CH_3)_2NH_2][Zr(PO_4)F_2]$ represents the first crystalline inorganic zirconium phosphate fluoride ion exchange material for radionuclide capture. This work provides a high-performance ion exchanger as a candidate for radiostrontium capture.

Received 8th August 2025,
Accepted 19th September 2025

DOI: 10.1039/d5ce00784d

rsc.li/crystengcomm

Introduction

Strontium-90 (^{90}Sr), recognized as one of the most hazardous artificial radionuclides, predominantly exists as $^{90}Sr^{2+}$ ions in radioactive waste liquids. As a β-emitting radioisotope derived from the nuclear fission of $^{235}U/^{239}Pu$, ^{90}Sr exhibits a long half-life ($t_{1/2}$ = 28.6 years) and high β-particle energy (0.546 MeV),[1,2] posing severe environmental and health risks due to its high mobility, radiotoxicity, and biotoxicity.[3,4] Its chemical similarity to Ca^{2+} facilitates bioaccumulation in human bone tissues, leading to bone cancer and leukemia.[5,6] On the other hand, ^{90}Sr has found significant implementation in therapeutic oncology as a radiation source for targeted bone cancer treatment.[7] Concurrently, its sustained decay heat generation enables essential roles in radioisotope thermoelectric generators (RTGs), particularly for powering deep-space probes and remote terrestrial monitoring systems under extreme environmental conditions.[7,8] Thus, the rapid separation and recovery of ^{90}Sr are critical for radioactive waste management, human health protection, environmental sustainability, and resource recycling.[7] However, ^{90}Sr waste liquids are extremely complex, typically containing abundant non-radioactive ions (*e.g.*, Na^+, K^+, and Mg^{2+}) and other fission products.[9] Therefore, highly selective capture of Sr^{2+} from such complex radioactive matrices remains a significant challenge.

Current strategies for Sr^{2+} removal include solvent extraction,[10,11] chemical precipitation,[12] and adsorption/ion exchange.[13] Among these, adsorption/ion exchange stands out for its cost-effectiveness, operational simplicity, and high efficiency.[14,15] Various ion exchange materials have been widely studied, such as zeolites,[16] layered clay minerals,[17] crystalline silicotitanates,[18] porous coordination polymers,[19] and metal chalcogenides.[20,21] Particularly, inorganic ion exchangers demonstrate potential for radionuclide remediation due to their structural robustness under extreme conditions.[22] Metal phosphate compounds have employed as ion exchange materials for Sr^{2+} ion capture, attributed to their good thermostability, radiation resistance,[23] and inherent selective coordination capacity of phosphate groups toward multivalent cations.[23–25] Specifically, tetravalent metal orthophosphates exhibit superior ion exchange characteristics, particularly in nuclear waste treatment scenarios due to their thermal stability, radiation tolerance, and structural stability under acidic conditions.[23,25–29]

[a] *College of Chemistry and Materials Science, Fujian Normal University, Fuzhou 350007, P. R. China*
[b] *State Key Laboratory of Structural Chemistry, Fujian Institute of Research on the Structure of Matter, Chinese Academy of Sciences, Fuzhou 350002, P. R. China. E-mail: shy@fjirsm.ac.cn, fml@fjirsm.ac.cn*
[c] *Fujian College, University of Chinese Academy of Sciences, Fuzhou, 350002, P.R. China*

Zirconium phosphate (ZrP) and its structural analogues have been extensively studied as classical materials for Sr^{2+} capture.[25,30,31] However, most of them exhibit poor Sr^{2+} selectivity in excessive competitive ions (such as Na^+, K^+, and Ca^{2+}), severely compromising strontium capture.[32–35] For instance, crystalline α-$Zr(HPO_4)_2{\cdot}H_2O$ (α-ZrP) exhibits adsorption capacities of 64.10 mg g^{-1} for Cs^+ and 43.03 mg g^{-1} for Sr^{2+}.[32,33] Meanwhile, γ-$Zr(PO_4)H_2PO_4{\cdot}2H_2O$ (γ-ZrP) demonstrates enhanced uptake for both Rb^+ (129.90 mg g^{-1}) and Sr^{2+} (114.78 mg g^{-1}), though excessive Na^+/Ca^{2+} ions severely compromise strontium capture.[34] Kinetic analyses reveal that γ-ZrP's ion exchange rates follow the hierarchy of $Cs^+ > K^+ > Rb^+ > Sr^{2+}$. Recently, potassium-incorporated zirconium phosphate ($K_2Zr(PO_4)_2$) shows the Sr^{2+} capture property but with poor selectivity for Sr^{2+} due to the effect of competitive ions (Ca^{2+}, Na^+, and H^+).[35] Additionally, introducing fluorine into phosphate structures facilitates the formation of highly stable Zr–F bonds, enhancing crystallinity and thermal stability and improving structural diversity and robustness.[36] Nevertheless, crystalline inorganic zirconium phosphate fluoride has never been studied for the removal of radioactive ions.

In this work, a new crystalline zirconium phosphate fluoride $[(CH_3)_2NH_2][Zr(PO_4)F_2]$ is reported, which is characterized by a layered anionic framework of $[Zr(PO_4)F_2]_n^{n-}$ hosting intercalated $[(CH_3)_2NH_2]^+$ cations. It exhibits exceptional Sr^{2+} capture across wide pH regimes (1.95–8.46). It has a high Sr^{2+} adsorption capacity (q_m^{Sr} = 161.48 mg g^{-1}) and rapid capture kinetics (removal rate R^{Sr} = 94.89% within 1 min). Further, it maintains Sr^{2+} removal efficiency in the presence of competing Cs^+, K^+, Na^+, Ca^{2+}, and Mg^{2+} ions. It is also demonstrated that the material can efficiently capture Sr^{2+} from actual aqueous systems (especially seawater), surpassing most reported solid sorbents. This study highlights the substantial potential of layered crystalline zirconium phosphate fluorides for radionuclide capture, while establishing a rational design paradigm for developing Sr^{2+}-selective ion-exchange materials of crystalline zirconium phosphate fluorides.

Materials and methods

Materials

$ZrOCl_2{\cdot}8H_2O$ (98.00%, Shanghai Adamas Reagent Co., Ltd.), *N*,*N*-dimethylacetamide (abbreviated as DMA, AR, Sinopharm Chemical Reagent Co., Ltd.), 2-hydroxyphosphonoacetic acid (abbreviated as HPAA, 50%, Shanghai Adamas Reagent Co., Ltd.), hydrofluoric acid (abbreviated as HF, AR, ≥40 nt, Shanghai Adamas Reagent Co., Ltd.), HNO_3 (65–68%, China Pharmaceutical Chemical Reagents Co., Ltd.), NaOH (98.00%, Greagent Reagent Co., Ltd.), $SrCl_2{\cdot}6H_2O$ (AR, Guangfu Co., Ltd.), CsCl (99.99%, Shanghai Longjin Metal Materials Co., Ltd.), KCl (AR, Shanghai Titan Co., Ltd.), NaCl (AR, Sinopharm Chemical Reagent Co., Ltd.), $CaCl_2{\cdot}2H_2O$ (74–78%, Shanghai Songjiang Silian Chemical Co., Ltd.), $MgCl_2{\cdot}6H_2O$ (AR, Kelong Co., Ltd.). Ultrapure water was supplied by a certified laboratory water purification system (Model WP-UP-LH-10, Sichuan Water Treatment Equipment Co., Ltd.). All reagents were purchased directly for use without further purification.

Synthesis of $[(CH_3)_2NH_2][Zr(PO_4)F_2]$

$[(CH_3)_2NH_2][Zr(PO_4)F_2]$ was synthesized through a solvothermal process using stoichiometric quantities of $ZrOCl_2{\cdot}8H_2O$ (2.4 mmol, 0.7735 g) and HPAA (2.4 mmol, 0.3745 g) in a mixed solvent system containing DMA (24 mL) and deionized water (5 mL). To modulate crystallization kinetics, HF (0.08 mL) was introduced as a mineralizer.[37] The reaction mixture was then acidified to pH 4 through precise addition of HNO_3 (1 mL), a critical parameter influencing layer assembly.

After homogenization *via* magnetic stirring at ambient temperature, the precursor solution was transferred to a 100 mL Teflon-lined autoclave and subjected to thermal treatment at 200 °C for 72 h under autogenous pressure. This prolonged aging period facilitated the formation of well-defined crystalline phases.

The resultant crystals were isolated by vacuum filtration, followed by sequential washing cycles with deionized water and ethanol (3 × 20 mL each) to remove residual organics. Subsequently, drying under ambient conditions yielded the target compound $[(CH_3)_2NH_2][Zr(PO_4)F_2]$ (relative molecular mass (M) = 270.28 g mol^{-1}) as colorless plate-like crystals, where $[(CH_3)_2NH_2]^+$ was generated by the thermal decomposition of DMA as the starting material and $(PO_4)^{3-}$ was generated by the thermal decomposition of HPAA.[38] Yield: 20.13% (calculated based on Zr content). Elemental analysis (EA) validated phase purity: theoretical: C 9.02%, H 3.03%, N 5.26%. Experimental: C 8.97%, H 3.33%, N 4.83%.

Batch adsorption experiment

The adsorption performance evaluation of $[(CH_3)_2NH_2][Zr(PO_4)F_2]$ was conducted in 25 mL polyethylene bottles with caps at room temperature. The experimental setup included: phase allocation, precise dosing of $[(CH_3)_2NH_2][Zr(PO_4)F_2]$ (solid–liquid ratio m/V = 1 g L^{-1}) and Sr^{2+} standard solution into bottles, followed by continuous agitation on a magnetic stirrer for 12 h at ambient temperature. Post-adsorption, aliquots of the supernatant were extracted *via* syringe, filtered through 0.22 μm membranes, and diluted with 2% HNO_3 prior to Sr^{2+} concentration analysis by ICP-OES or ICP-MS. The post-adsorption solid phase was isolated from the aqueous medium *via* centrifugal separation at 8000 rpm for 10 min, followed by triple rinsing with deionized water to eliminate residual ions prior to subsequent analysis.

The Sr^{2+}-exchanged derivative of $[(CH_3)_2NH_2][Zr(PO_4)F_2]$ (designated as $[(CH_3)_2NH_2][Zr(PO_4)F_2]$-Sr) was synthesized *via* 12 h room-temperature agitation of 200 mg adsorbent in 200 mL of Sr^{2+} solution. The resultant $[(CH_3)_2NH_2][Zr(PO_4)F_2]$-Sr underwent comprehensive characterization (PXRD, EDS,

SEM, and EA). Experimental particulars are described in the supplementary information (SI).

Characterization techniques

Elemental composition (C, H, N) was quantified *via* high-precision combustion analysis using a Vario EL III EA. Single-crystal X-ray diffraction analysis of $[(CH_3)_2NH_2][Zr(PO_4)F_2]$ was performed on a Rigaku XtaLAB Synergy-R diffractometer equipped with a graphene-monochromated microfocus Mo K_α radiation source (λ = 0.71073 Å) at 100 K. Powder X-ray diffraction (PXRD) patterns were acquired at room temperature on a Rigaku Miniflex II system equipped with Cu K_α radiation (λ = 1.54178 Å), operating at 30 kV and 15 mA, with a 2θ scanning range of 5–65°. Elemental composition and spatial distribution were analyzed by energy-dispersive X-ray spectroscopy (EDS) coupled with scanning electron microscopy (SEM, JEOL JSM-6700F). Surface chemical states were investigated *via* X-ray photoelectron spectroscopy (XPS) on a ThermoFisher ESCALAB 240 Xi spectrometer using monochromatic Al K_α excitation. Solution pH measurements were conducted with a Leimage E-201F digital pH meter (Shanghai, China). The concentration of Sr^{2+} and other metal ions were quantificationally measured by inductively coupled plasma optical emission spectroscopy (ICP-OES, Thermo iCAP 7400) and inductively coupled plasma mass spectrometry (ICP-MS, Thermo XSeries II), respectively. Liquid–solid separation was achieved *via* centrifugation using a G16-WS benchtop centrifuge.

Results and discussion

Crystal structures

Single-crystal X-ray diffraction (SC-XRD) analysis determines that $[(CH_3)_2NH_2][Zr(PO_4)F_2]$ crystallizes in the monoclinic space group $P2_1/m$. The asymmetric unit comprises one Zr atom, one PO_4 group, two F atoms, and one $[(CH_3)_2NH_2]^+$ cation (Fig. S1). The Zr center adopts a distorted octahedral geometry, coordinated by four oxygen donors from distinct PO_4 groups (Zr–O: 2.054–2.079 Å) and two F atoms (Zr–F: 1.972–2.007 Å). The bond angles span 86.6(3)–93.5(3)° for O–Zr–F and 88.89(10)–91.11(10)° for O–Zr–O, reflecting minor octahedral distortion (Tables S1–S3).

Alternating arrangements of ZrO_4F_2 octahedra and PO_4 tetrahedra by corner-sharing mode generate a 2D anionic layer of $[Zr(PO_4)F_2]_n^{n-}$, in which each ZrO_4F_2 octahedron connects four PO_4 tetrahedra and each PO_4 tetrahedron links four ZrO_4F_2 octahedra (Fig. 1a). It is found that an eight-membered ring (8-MR) window with dimensions 4.63 × 5.04 Å is formed by two Zr atoms, two P atoms, and four O atoms in the anionic layer (Fig. 1b). Charge-balancing $[(CH_3)_2NH_2]^+$ cations are intercalated between adjacent layers (Fig. 1c and d), with an interlayer spacing of 7.60 Å (defined as the shortest perpendicular distance between Zr atom of adjacent anionic layers, as defined in Fig. S1).[39] The relatively big interlamellar spacing and the presence of exchangeable

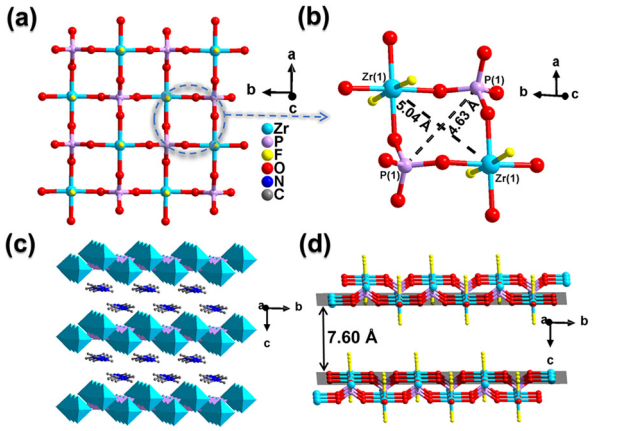

Fig. 1 Crystal structural diagrams for the compound $[(CH_3)_2NH_2][Zr(PO_4)F_2]$. (a) A 2D anionic layer of $[Zr(PO_4)F_2]_n^{n-}$ viewed along the *c*-axis. (b) Ball-and-stick representation of the eight-membered ring in the anionic layer. (c) View of the packing diagram of $[(CH_3)_2NH_2][Zr(PO_4)F_2]$ along the *a*-axis. (d) The anionic $[Zr(PO_4)F_2]_n^{n-}$ layers arrangement illustrating interlayer spacing (7.60 Å). Color scheme: Zr (cyan), P (purple), O (red), F (yellow), N (blue), C (grey).

$[(CH_3)_2NH_2]^+$ cations provide the prerequisite for the Sr^{2+} capture *via* the ion exchange way.[40]

Adsorption isotherms studies

Adsorption isotherm analysis serves as a fundamental methodology for characterizing the surface characteristics and binding affinity of adsorbents, while also determining their maximum adsorption capacity (q_m^{Sr}). The actual and theoretical (assuming that all available $[(CH_3)_2NH_2]^+$ is fully exchanged by Sr^{2+}) ion-exchange capacity is calculated by eqn (S1) and eqn (S2). The Sr^{2+} ions adsorption capacity of $[(CH_3)_2NH_2][Zr(PO_4)F_2]$ was systematically evaluated through equilibrium isotherm studies. Experimental data were modeled using three classical adsorption isotherms: Langmuir (monolayer adsorption), Freundlich (heterogeneous surface), and Langmuir–Freundlich hybrid (multi-mechanism synergy).[41] Nonlinear regression analysis reveals superior correlation for the Langmuir–Freundlich model (R^2 = 0.9858) compared to the Langmuir (R^2 = 0.9699) and Freundlich (R^2 = 0.8467) models (Fig. 2a, Tables S4 and S5, and eqn (S3)–(S5)). This statistical dominance indicates a complex adsorption mechanism involving both monolayer coverage and heterogeneous surface interactions.[41] The derived q_m^{Sr} from the Langmuir–Freundlich model reaches 161.48 mg g^{-1}, which is higher than that of some crystalline zirconium-based adsorbents such as zirconium fluorophosphonate $[(CH_3)_2NH_2]_2[ZrC_6H_4(CH_2PO_3)_2F_2]$ (SZ-7, 129.1 mg g^{-1}), $[(CH_3)_2NH_2][ZrCH_2(PO_3)_2F]$ (SZ-4, 121 mg g^{-1}),[42] and zirconium phosphates such as γ-ZrP (114.78 mg g^{-1}), $K_2Zr(PO_4)_2$ (52.83 mg g^{-1}), and α-ZrP (43.03 mg g^{-1}), as visually compared in Table S6 and Fig. 2b.[20,21,42–46] Furthermore, the title compound $[(CH_3)_2NH_2][Zr(PO_4)F_2]$ also outperforms some other inorganic adsorbents

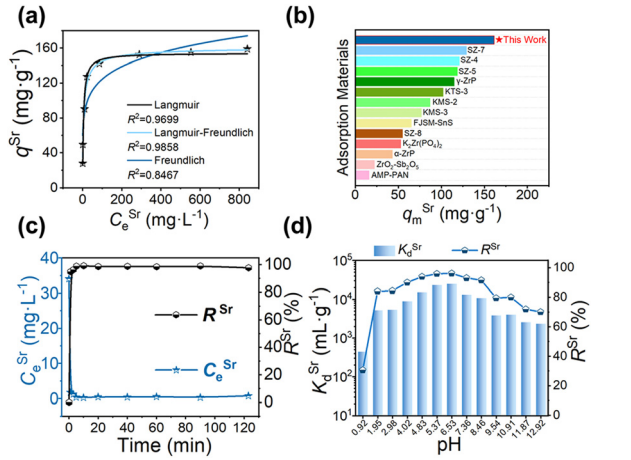

Fig. 2 Adsorption performance diagrams of the compound $[(CH_3)_2NH_2][Zr(PO_4)F_2]$. (a) Sr^{2+} adsorption isotherms of $[(CH_3)_2NH_2][Zr(PO_4)F_2]$ fitted by the Langmuir (black line), Langmuir–Freundlich (azure line), and Freundlich (blue line) models. (b) Comparison of the adsorption capacities of $[(CH_3)_2NH_2][Zr(PO_4)F_2]$ with other reported inorganic adsorbents for Sr^{2+}. (c) The kinetic curves of Sr^{2+} removal rate (R) by $[(CH_3)_2NH_2][Zr(PO_4)F_2]$ plotted as the concentration (C_e) and R^{Sr} of Sr^{2+} ions *vs.* time (min). (d) Distribution coefficient (K_d^{Sr}, columns) and removal rate (R^{Sr}, line) at various solutions with different initial pH (0.92–12.92).

such as $K_{2x}Sn_{4-x}S_{8-x}$ (x = 0.65–1) (KTS-3, 102.00 mg g^{-1})[47] and commercial AMP–PAN (16 mg g^{-1}).[48]

Adsorption kinetics studies

The rapid capture capability of an adsorption material for radioactive Sr^{2+} ions is critical in nuclear emergency management. $[(CH_3)_2NH_2][Zr(PO_4)F_2]$ demonstrated exceptional adsorption efficiency, achieving a Sr^{2+} removal rate of 94.89% within 1 min in neutral aqueous solutions (Sr^{2+} concentration: from 34.04 mg L^{-1} to 1.74 mg L^{-1}, Fig. 2c, Table S7, eqn (S6)). The current compound approached adsorption equilibrium within a 5 min contact period, achieving remarkable Sr^{2+} removal efficiency (R^{Sr} = 98.88%). We systematically investigated the Sr^{2+} adsorption mechanism of it using pseudo-first-order and pseudo-second-order kinetic models (Table S8, Fig. S2, eqn (S7) and (S8)).[49] Quantitative analysis demonstrated superior correlation with the pseudo-second-order kinetic model.

pH effect on adsorption

The pH of aqueous solutions critically governs adsorption processes by mediating proton competition and material stability. To systematically evaluate these effects, the removal performance of $[(CH_3)_2NH_2][Zr(PO_4)F_2]$ was investigated across a pH range of 0.92–12.92 (Fig. 2d, Table S9, eqn (S9)). The title compound exhibited exceptional adsorption capacities across the pH range of 1.95–8.46, with distribution coefficients (K_d^{Sr}) consistently exceeding 5 × 10^3 mL g^{-1} and R^{Sr} above 83.99%, accompanied by a moderate leaching of Zr (Fig. S3a). The leaching rates of Zr of $[(CH_3)_2NH_2][Zr(PO_4)F_2]$ after being immersed in different acidic (pH of 1.95) or alkaline (pH of 11.87) solutions for 12 h were less than 6.60% (Fig. S3a). At pH 1.95–12.92, the layered anionic architecture of $[Zr(PO_4)F_2]_n^{n-}$ is stable, as no phase transition observed by PXRD (Fig. S3b). This indicates that $[(CH_3)_2NH_2][Zr(PO_4)F_2]$ has relatively wide acid–base stability. Under strongly acidic conditions (pH = 0.92), K_d^{Sr} exhibits a substantial reduction to 4.4 × 10^2 mL g^{-1}, possibly attributed to competitive proton exchange, where H^+ effectively displaces Sr^{2+} at $[(CH_3)_2NH_2]^+$ sites. Under extreme acidity, concomitantly partially structural degradation of the anionic layers further diminished the ion-exchange capacity.[30] Subsequently, we employed the pH drift method for analysing the pH dependence of adsorption. The ΔpH (= pH_0 − pH_f) *vs.* pH_0 curve shows the pH_{pzc} value of 5.0 (Fig. S3c). It indicates that the surface of $[(CH_3)_2NH_2][Zr(PO_4)F_2]$ is positively charged at pH < 5.0 and negatively charged at pH > 5.0. For low pH, the surface of $[(CH_3)_2NH_2][Zr(PO_4)F_2]$ favours electrostatic attraction of anions, while for high pH, it favours the attraction of cations.

Competitive adsorption

The presence of high-concentration competing ions (Na^+, K^+, Mg^{2+}, and Ca^{2+}) poses significant challenges for selective Sr^{2+} removal in nuclear wastewater treatment. Thus, we systematically evaluated the Sr^{2+} selectivity of $[(CH_3)_2NH_2][Zr(PO_4)F_2]$ under competing ions (Na^+, K^+, Cs^+, Mg^{2+}, and Ca^{2+}) using separation factor (SF) and distribution coefficient (K_d) analyses. Notably, effective SF typically requires values exceeding 100.[50]

Competitive impacts of individual competitive Na^+, K^+, and Mg^{2+} ions concentrations on Sr^{2+} adsorption by $[(CH_3)_2NH_2][Zr(PO_4)F_2]$ were quantified. At the Na^+/Sr^{2+} molar ratio of 494.4 : 1, it maintains Sr^{2+} removal efficiency of 99.37% (K_d^{Sr} = 1.59 × 10^5 mL g^{-1}, $SF_{Sr/Na}$ = 2219.95), confirming excellent Na^+/Sr^{2+} separation (Fig. 3a, Table S10, eqn (S10)). At the K^+/Sr^{2+} molar ratio of 45.6 : 1, K_d^{Sr} reaches 3.96 × 10^4 mL g^{-1} with R^{Sr} of 97.54% (Fig. 3b, Table S11). Even under extremely excessive K^+ (C_0^{Sr} = 5.57 mg L^{-1}, C_0^K = 294.91 mg L^{-1}, K^+/Sr^{2+} molar ratio of 118.7 : 1), K_d^{Sr} reaches 2.69 × 10^4 mL g^{-1} (R^{Sr} = 96.41%). Notably, $SF_{Sr/K}$ surpasses 100, confirming exceptional selectivity for Sr^{2+} over competing K^+ ions. At the Mg^{2+}/Sr^{2+} molar ratio of 20.1 : 1, K_d^{Sr} remains 1.17 × 10^5 mL g^{-1} (R^{Sr} = 99.15%, $SF_{Sr/Mg}$ = 299.98), underscoring $[(CH_3)_2NH_2][Zr(PO_4)F_2]$'s resilience against the interference of alkaline earth metal ions (Fig. 3c, Table S12). However, when the Mg^{2+}/Sr^{2+} molar ratios are more than 211.4 : 1, the Sr^{2+} removal of the current compound is interfered.[51]

Simultaneously, Sr^{2+} selectivity of $[(CH_3)_2NH_2][Zr(PO_4)F_2]$ was systematically evaluated in mixed Na^+, K^+, Cs^+, and Sr^{2+} solution and mixed Cs^+, K^+, Na^+, Ca^{2+}, Mg^{2+}, and Sr^{2+} solution (Fig. 3d and e, Tables S13 and S14), respectively. In the mixed Na^+, K^+, Cs^+, and Sr^{2+} solution, the material exhibits exceptionally high separation factors ($SF_{Sr/M}$ > 100, M = Na^+

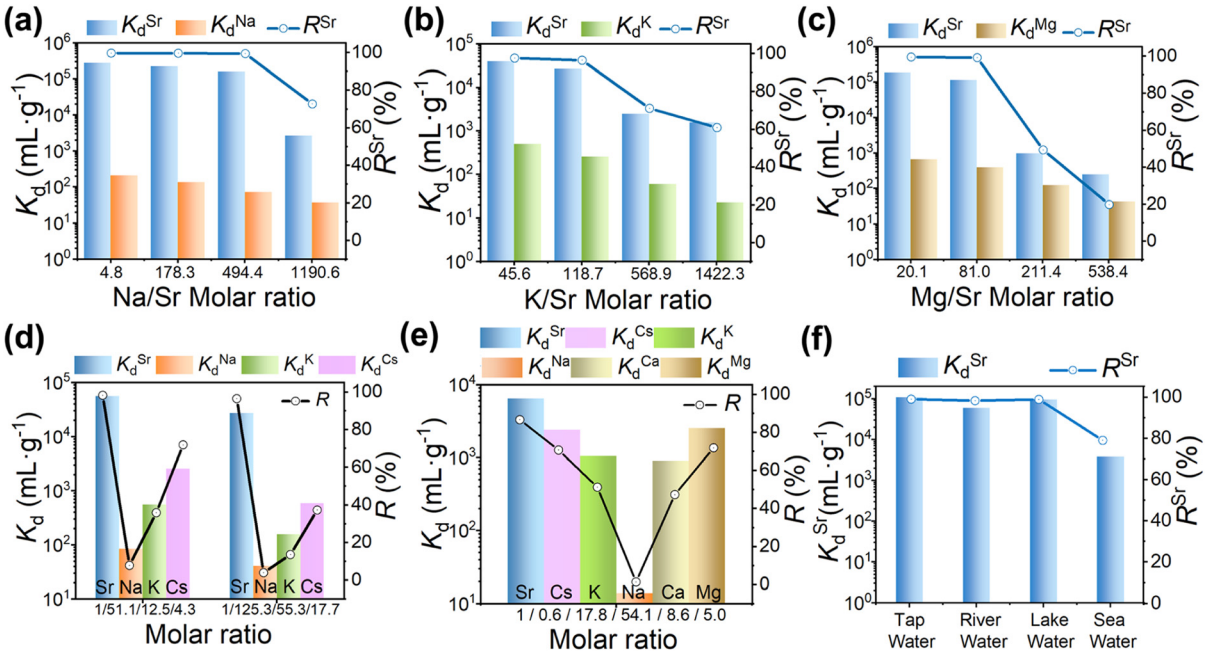

Fig. 3 Selectivity performance diagrams of the compound $[(CH_3)_2NH_2][Zr(PO_4)F_2]$. K_d (columns) for Sr^{2+}, K^+, Na^+, Mg^{2+} and R^{Sr} (line plot) of $[(CH_3)_2NH_2][Zr(PO_4)F_2]$ at different molar ratios of Na/Sr (a), K/Sr (b), and Mg/Sr (c). (d) K_d for Sr^{2+}, K^+, Na^+, Cs^+ and R^{Sr} of $[(CH_3)_2NH_2][Zr(PO_4)F_2]$ in mixed Na^+, K^+, Cs^+, and Sr^{2+} solution at different molar ratios. (e) K_d for various metal ions and R^{Sr} of $[(CH_3)_2NH_2][Zr(PO_4)F_2]$ in mixed Cs^+, K^+, Na^+, Ca^{2+}, Mg^{2+}, and Sr^{2+} solution. (f) K_d^{Sr} and R^{Sr} of $[(CH_3)_2NH_2][Zr(PO_4)F_2]$ in tap water, river water, lake river, and sea water.

and K^+) for Sr^{2+} under the presence of monovalent competing ions. $SF_{Sr/M}$ (M = Na^+, K^+) exceed 668.67 and 173.09 despite the presence of high concentrations for competing ions, whereas $SF_{Sr/Cs}$ is merely 45.66. Nevertheless, in the mixed Cs^+, K^+, Na^+, Ca^{2+}, Mg^{2+}, and Sr^{2+} solution, significantly diminished selectivity ($SF_{Sr/M} < 100$, M = K^+, Cs^+, Mg^{2+}, and Ca^{2+}) was observed in monovalent and divalent cation matrices. Remarkably, $SF_{Sr/Na}$ values still remain elevated (464.99) with concurrent high distribution coefficient (K_d^{Sr} = 6.44×10^3 mL g^{-1}) and removal efficiency (R^{Sr} = 86.57%).

Significantly, further validation in actual aqueous environments including tap water, lake water, river water, and seawater demonstrates consistently high R^{Sr} values of 99.09%, 98.34%, 98.97%, and 79.06%, respectively, while K_d^{Sr} values exceed 3.78×10^3 mL g^{-1} without exception (Fig. 3f, Table S15). The removal rate in actual seawater is higher than that of many reported adsorbents, such as K_2SbPO_6 (R^{Sr} = 1.17%)[52] and K-HTNs (R^{Sr} = 35%)[53] at m/V = 1 g L^{-1}. These results unequivocally establish the maintenance of the removal capacity of $[(CH_3)_2NH_2][Zr(PO_4)F_2]$ in complex contaminated matrices.

Adsorption and desorption

Reusability serves as a critical performance for ion exchange materials. Remarkably, the Sr-loaded phase $[(CH_3)_2NH_2][Zr(PO_4)F_2]$-Sr can be efficiently reused through elution with a 0.5 mol L^{-1} KCl solution. The sample treated with KCl solution is named $[(CH_3)_2NH_2][Zr(PO_4)F_2]$-Sr-K. EDS analysis of the eluted material confirms near-complete substitution of Sr^{2+} by K^+ ions (Fig. S4a and b). The eluted material still maintains exceptional Sr^{2+} adsorption capacity (R^{Sr} = 93.80%) over one adsorption–desorption cycle, with high desorption efficiencies (E^{Sr} = 91.47%) (Table S16, eqn (S11)). Structural integrity preservation is verified through PXRD patterns in cycled samples (Fig. S4c). $[(CH_3)_2NH_2][Zr(PO_4)F_2]$ demonstrates reusability capabilities for the sequential capture of Sr^{2+} ions in radioactive waste management.

Adsorption mechanism

PXRD analysis validates no detectable phase transitions observed upon Sr^{2+} displacement (Fig. S5). Notably, the (002) diffraction peak of $[(CH_3)_2NH_2][Zr(PO_4)F_2]$-Sr shifts toward higher Bragg angles ($\Delta 2\theta$ = 0.46°) according to the Bragg equation. Corresponding SEM characterization reveals well-defined $[(CH_3)_2NH_2][Zr(PO_4)F_2]$-Sr crystals exhibiting pristine morphological integrity, evidenced by defect-free planar facets (Fig. S6).

Based on the above evidences, we hypothesized that this follows the ion exchange mechanism, wherein $[(CH_3)_2NH_2]^+$ cations are displaced by Sr^{2+} (Fig. 4a). To validate this hypothesis, high-resolution XPS analysis of the pristine and Sr-loaded phases was conducted. All XPS spectra were corrected to the C 1s peak of adventitious carbon at 284.8 eV. XPS spectra reveal Sr 3d and P 2p signals overlap at ~133.0 eV in $[(CH_3)_2NH_2][Zr(PO_4)F_2]$-Sr (Fig. 4b),[54] while emergent peaks at 360.0 eV (Sr 3s) and 270.0 eV (Sr 3p) provide unambiguous evidence of strontium integration, accompanied by definitive Sr 3d spectral signatures at

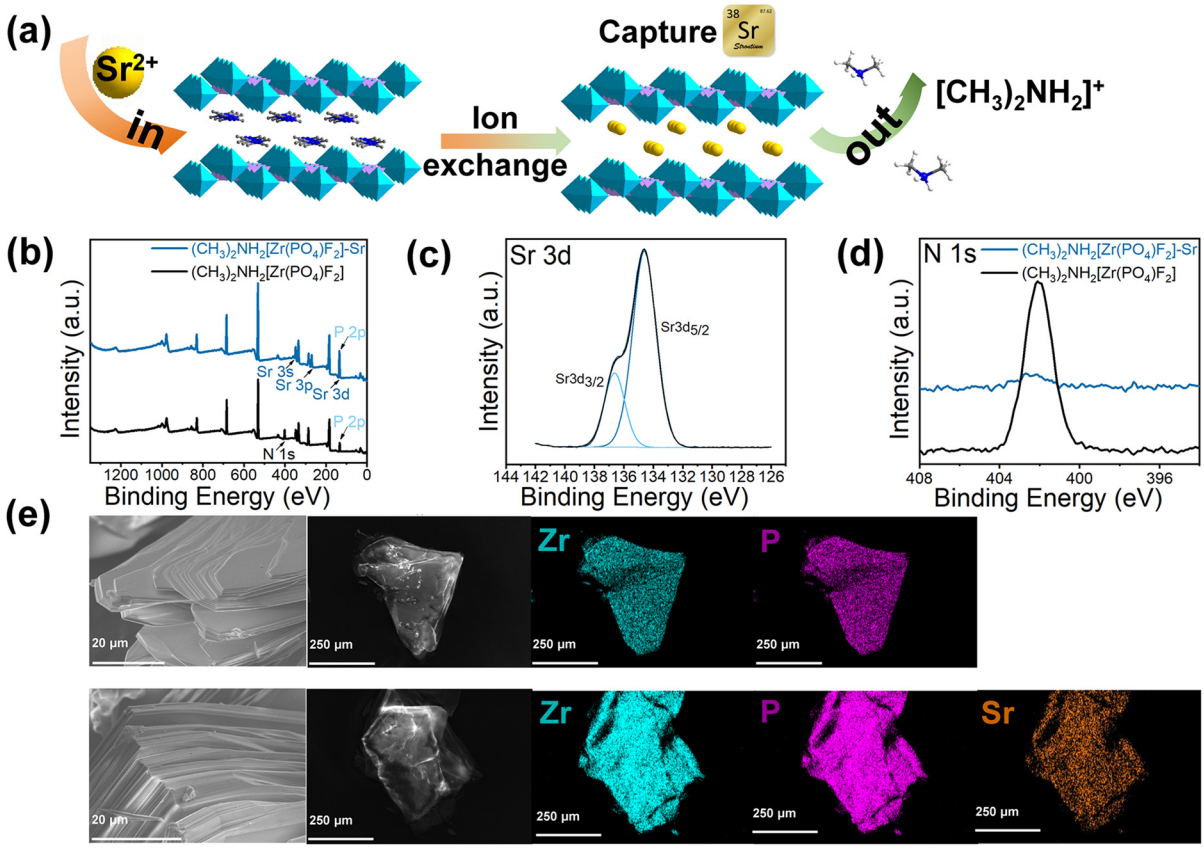

Fig. 4 Adsorption mechanism diagrams of the compound $[(CH_3)_2NH_2][Zr(PO_4)F_2]$. (a) Mechanistic illustration of Sr^{2+} exchange within the anionic layers of $[(CH_3)_2NH_2][Zr(PO_4)F_2]$. (b) Comparative XPS survey spectra of pristine $[(CH_3)_2NH_2][Zr(PO_4)F_2]$ (black) and $[(CH_3)_2NH_2][Zr(PO_4)F_2]$-Sr (blue). (c) Narrow scan XPS spectrum of Sr 3d of $[(CH_3)_2NH_2][Zr(PO_4)F_2]$-Sr. (d) Narrow scan XPS spectra of N 1s in pristine $[(CH_3)_2NH_2][Zr(PO_4)F_2]$ (black) *versus* $[(CH_3)_2NH_2][Zr(PO_4)F_2]$-Sr (blue). (e) SEM micrographs at magnification of 2.0k, complemented by corresponding elemental distribution profiles of pristine $[(CH_3)_2NH_2][Zr(PO_4)F_2]$ and $[(CH_3)_2NH_2][Zr(PO_4)F_2]$-Sr.

binding energies of 134.6 eV (Sr $3d_{5/2}$), 136.6 eV (Sr $3d_{3/2}$) (Fig. 4c). At the same time, N 1s intensity attenuated at 402.1 eV after Sr^{2+} capture (Fig. 4d). Collectively, these results confirm that Sr^{2+} capture occurs *via* ion exchange between interlamellar $[(CH_3)_2NH_2]^+$ cations and Sr^{2+}.

EDS analysis (Fig. S6f) confirmed successful capture of Sr^{2+} ions. Elemental mapping reveals a homogeneous distribution of Sr^{2+} in $[(CH_3)_2NH_2][Zr(PO_4)F_2]$-Sr (Fig. 4e). EA further reveals a concomitant reduction in nitrogen content from 4.83% to 0.43% after Sr^{2+} ion exchange (experimental: C 1.50%, H 2.11%, N 0.43%), quantitatively confirming that $[(CH_3)_2NH_2]^+$ ions have been exchanged during ion exchange. Furthermore, the theoretical ion exchange capacity of $[(CH_3)_2NH_2][Zr(PO_4)F_2]$ for Sr^{2+} is calculated as 162.10 mg g^{-1} (eqn (S2)), whereas by experimental measurements the adsorption capacity of $[(CH_3)_2NH_2][Zr(PO_4)F_2]$ for Sr^{2+} is 161.48 mg g^{-1}. This indicates that the interlamellar $[(CH_3)_2NH_2]^+$ cations are almost completely exchanged by Sr^{2+} ions.

In simulated nuclear wastewater containing competing ions (Na^+, K^+, Cs^+, Ca^{2+}, and Mg^{2+}), $(CH_3)_2NH_2[Zr(PO_4)F_2]$ maintained Sr^{2+} removal efficiency. Ion exchange constitutes a stoichiometrically constrained process wherein charge balance is preserved through equivalent substitution of exchanged cations.[55] The Sr^{2+} selectivity of $(CH_3)_2NH_2[Zr(PO_4)F_2]$ may arise from the electrostatic valence-dependency rule: adsorbent affinity scales with cation charge density under constant selectivity coefficients and concentrations of competing cations.[56] Consequently, the $[Zr(PO_4)F_2]_n^{n-}$ anionic layers may exhibit preferential binding toward divalent Sr^{2+} over monovalent Na^+/K^+. This material achieves $SF_{Sr/Mg}$ exceeding 100, possibly because the hydrated Sr^{2+} diameter (8.24 Å) is smaller than competing cations (Mg^{2+}, 8.56 Å).[51]

Thermodynamics of Sr^{2+} adsorption on $[(CH_3)_2NH_2][Zr(PO_4)F_2]$ was further investigated between 293–353 K (Table S17, Fig. S7). The K_d values increased with temperature, indicating enhanced adsorption affinity at higher temperatures. The thermodynamic parameters were also calculated using the thermodynamic model (eqn (S13)–(S15)).[57,58] Thermodynamic parameters reveal positive ΔH^0 (29.62 kJ mol^{-1}) and ΔS^0 (0.18 kJ mol^{-1} K^{-1}), confirming an entropy-driven process. Negative ΔG^0 values (−22.10 to −32.55 kJ mol^{-1}) demonstrate spontaneous adsorption across the temperature range. The decreasing ΔG^0 with rising temperature further support favourable

adsorption at elevated temperatures. Notably, operational expenditure increases at higher temperatures, necessitating balanced temperature selection.

Conclusions

Here, a new layered zirconium phosphate fluoride ($[(CH_3)_2NH_2][Zr(PO_4)F_2]$) was synthesized hydrothermally. This material achieves a maximum Sr^{2+} adsorption capacity of 161.48 mg g^{-1} (higher than that of many inorganic crystalline adsorbents) and fast kinetics (R^{Sr} = 94.89% within 1 min). It exhibits exceptional pH tolerance (operational range: 1.95–8.46). This material maintains Sr^{2+} removal efficiency in the presence of competing Cs^+, K^+, Na^+, Ca^{2+}, and Mg^{2+} ions. Particularly, it can maintain R^{Sr} of 79.06% even in seawater. XPS and thermodynamics confirm that spontaneous Sr^{2+} adsorption occurs through ion exchange with interlayered $[(CH_3)_2NH_2]^+$ cations in the current zirconium phosphate fluoride. This work provides a promising adsorbent for capture of radiostrontium in radioactive waste management.

Author contributions

Z. Y. Chen: data curation, writing – reviewing and editing, validation, formal analysis, investigation, and software. S. Z. Liu: formal analysis and data curation. S. J. Li: formal analysis. Z. H. Chen: formal analysis and visualization. L. Yang: data curation. S. M. Zhang: data curation. H. Y. Sun: funding acquisition, reviewing and editing, supervision, and project administration. M. L. Feng: conceptualization, funding acquisition, review and editing, visualization, supervision, and project administration. X. Y. Huang: review and editing, and project administration. All authors have read and agreed to the published version of the manuscript.

Conflicts of interest

The authors declare no conflict of interest.

Data availability

Supplementary information: experimental section (batch adsorption experiments, equations, crystal structures section, and characterization section), and additional tables (Tables S1–S17) and figures (Fig. S1–S7). See DOI: **https://doi.org/10.1039/D5CE00784D**.

CCDC 2466544 contains the supplementary crystallographic data for this paper.[59]

Acknowledgements

This research was funded by the National Natural Science Foundation of China (No. 22325605, U21A20296, and 22406185), the Natural Science Foundation of Fujian Province (No. 2024J08105), and the Strategic Priority Research Program of the Chinese Academy of Sciences (No. XDB1170000).

Notes and references

1 E. A. Martell, *Science*, 1959, **129**, 1197–1206.
2 J. Veliscek-Carolan, *J. Hazard. Mater.*, 2016, **318**, 266–281.
3 J. Zhang, L. Chen, X. Dai, L. Zhu, C. Xiao, L. Xu, Z. Zhang, E. V. Alekseev, Y. Wang, C. Zhang, H. Zhang, Y. Wang, J. Diwu, Z. Chai and S. Wang, *Chem*, 2019, **5**, 977–994.
4 F. Zhang, J. Wang, Q. Bi and J. Du, *Sci. Total Environ.*, 2021, **764**, 144266.
5 S. Pors Nielsen, *Bone*, 2004, **35**, 583–588.
6 T. L. Gerke, B. J. Little, T. P. Luxton, K. G. Scheckel and J. B. Maynard, *Environ. Sci. Technol.*, 2013, **47**, 5171–5177.
7 J. Bruno and R. C. Ewing, *Elements*, 2006, **2**, 343–349.
8 R. C. O'Brien, R. M. Ambrosi, N. P. Bannister, S. D. Howe and H. V. Atkinson, *J. Nucl. Mater.*, 2008, **377**, 506–521.
9 S. Inan, *J. Radioanal. Nucl. Chem.*, 2022, **331**, 1137–1154.
10 D. R. Raut, P. K. Mohapatra and V. K. Manchanda, *Sep. Sci. Technol.*, 2010, **45**, 204–211.
11 S. Kumar and R. V. S. Rao, *J. Radioanal. Nucl. Chem.*, 2021, **329**, 351–357.
12 X. Luo, G. Zhang, X. Wang and P. Gu, *J. Radioanal. Nucl. Chem.*, 2013, **298**, 931–939.
13 J. Tang, M. Feng and X. Huang, *Fundam. Res.*, 2024, DOI: **10.1016/j.fmre.2023.10.022**.
14 P. Kumar, A. Pournara, K.-H. Kim, V. Bansal, S. Rapti and M. J. Manos, *Prog. Mater. Sci.*, 2017, **86**, 25–74.
15 J. H. Tang, H. Y. Sun, W. Ma, M. L. Feng and X. Y. Huang, *Chin. J. Struct. Chem.*, 2020, **39**, 2157–2171.
16 I. Smiciklas, S. Dimovic and I. Plecas, *Appl. Clay Sci.*, 2007, **35**, 139–144.
17 A. F. Seliman, Y. F. Lasheen, M. A. E. Youssief, M. M. Abo-Aly and F. A. Shehata, *J. Radioanal. Nucl. Chem.*, 2014, **300**, 969–979.
18 S. Chitra, A. G. Shanmugamani, R. Sudha, S. Kalavathi and B. Paul, *J. Radioanal. Nucl. Chem.*, 2017, **312**, 507–515.
19 B. Aguila, D. Banerjee, Z. M. Nie, Y. Shin, S. Q. Ma and P. K. Thallapally, *Chem. Commun.*, 2016, **52**, 5940–5942.
20 M. J. Manos, N. Ding and M. G. Kanatzidis, *Proc. Natl. Acad. Sci. U. S. A.*, 2008, **105**, 3696–3699.
21 X. H. Qi, K. Z. Du, M. L. Feng, J. R. Li, C. F. Du, B. Zhang and X. Y. Huang, *J. Mater. Chem. A*, 2015, **3**, 5665–5673.
22 G. Alberti and U. Costantino, *J. Chromatogr.*, 1974, **102**, 5–29.
23 G. Alberti, M. Casciola, U. Costantino and R. Vivani, *Adv. Mater.*, 1996, **8**, 291–303.
24 P. Bhanja, J. Na, T. Jing, J. J. Lin, T. Wakihara, A. Bhaumik and Y. Yamauchi, *Chem. Mater.*, 2019, **31**, 5343–5362.
25 A. Clearfield and J. A. Stynes, *J. Inorg. Nucl. Chem.*, 1964, **26**, 117–129.
26 G. Alberti, M. Casciola, U. Costantino and M. L. Luciani, *J. Chromatogr.*, 1976, **128**, 289–299.
27 U. Costantino and A. Gasperon, *J. Chromatogr.*, 1970, **51**, 289–296.
28 X. F. Lu, Z. H. Chen, X. R. Shi, Q. Jing and M. H. Lee, *Angew. Chem., Int. Ed.*, 2020, **59**, 17648–17656.
29 N. Hirose and J. Kuwano, *J. Mater. Chem.*, 1994, **4**, 9–12.
30 Z. Q. Li, E. L. Vivas, Y. J. Suh and K. Cho, *J. Environ. Chem. Eng.*, 2022, **10**, 9.

31 W. J. Mu, Q. H. Yu, R. Zhang, X. L. Li, R. Hu, Y. He, H. Y. Wei, Y. Jian and Y. C. Yang, *J. Mater. Chem. A*, 2017, **5**, 24388–24395.
32 L. A. Wu, H. P. Wang, X. Q. Kong, H. B. Wei, S. Chen and L. S. Chi, *RSC Adv.*, 2023, **13**, 6346–6355.
33 J. Gu, S. Du, Q. Yu and W. Mu, *Huaxue Yanjiu Yu Yingyong*, 2020, **32**, 1067–1071.
34 Y. Cheng, I. bin Samsudin, S. Jaenicke and G. K. Chuah, *Chem. – Asian J.*, 2020, **15**, 3542–3550.
35 S. Bevara, P. Giri, S. J. Patwe, S. N. Achary, R. K. Mishra, A. Kumar, A. K. Sinha, C. P. Kaushik and A. K. Tyagi, *J. Environ. Chem. Eng.*, 2018, **6**, 2248–2261.
36 M. Wloka, S. Troyanov and E. Kemnitz, *J. Solid State Chem.*, 1998, **135**, 293–301.
37 N. Prasetyo and F. I. Pambudi, *Int. J. Hydrogen Energy*, 2021, **46**, 4222–4228.
38 M. Doskocz, S. Roszak, D. Majumdar, J. Doskocz, R. Gancarz and J. Leszczynski, *J. Phys. Chem. A*, 2008, **112**, 2077–2081.
39 R. L. C. Akkermans, N. A. Spenley and S. H. Robertson, *Mol. Simul.*, 2013, **39**, 1153–1164.
40 A. Bashir, S. Ahad, L. A. Malik, A. Qureashi, T. Manzoor, G. N. Dar and A. H. Pandith, *Ind. Eng. Chem. Res.*, 2020, **59**, 22353–22397.
41 K. Sakadevan and H. J. Bavor, *Water Res.*, 1998, **32**, 393–399.
42 J. R. Zhang, L. Chen, X. Dai, L. X. Chen, F. W. Zhai, W. F. Yu, S. K. Guo, L. J. Yang, L. H. Chen, Y. G. Zhang, L. W. He, C. L. Chen, Z. F. Chai and S. Wang, *Chem. Commun.*, 2021, **57**, 8452–8455.
43 J. R. Zhang, L. H. Chen, D. X. Gui, H. W. Zhang, D. Zhang, W. Liu, G. L. Huang, D. W. Juan, Z. F. Chai and S. Wang, *Dalton Trans.*, 2018, **47**, 5161–5165.
44 J. L. Mertz, Z. H. Fard, C. D. Malliakas, M. J. Manos and M. G. Kanatzidis, *Chem. Mater.*, 2013, **25**, 2116–2127.
45 J. Zhang, L. Chen, L. Chen, L. Chen, Y. Zhang, C. Chen, Z. Chai and S. Wang, *Dalton Trans.*, 2022, **51**, 14842–14846.
46 S. Inan and E. Nostar, *Sep. Sci. Technol.*, 2013, **48**, 1364–1369.
47 D. Sarma, C. D. Malliakas, K. S. Subrahmanyam, S. M. Islama and M. G. Kanatzidis, *Chem. Sci.*, 2016, **7**, 1121–1132.
48 Y. Park, Y. C. Lee, W. S. Shin and S. J. Choi, *Chem. Eng. J.*, 2010, **162**, 685–695.
49 Y. S. Ho, D. A. J. Wase and C. F. Forster, *Environ. Technol.*, 1996, **17**, 71–77.
50 Y. J. Gao, M. L. Feng, B. Zhang, Z. F. Wu, Y. Song and X. Y. Huang, *J. Mater. Chem. A*, 2018, **6**, 3967–3976.
51 E. R. Nightingale, *J. Phys. Chem.*, 1959, **63**, 1381–1387.
52 Y. L. Guo, H. Y. Sun, X. Zeng, T. T. Lv, Y. X. Yao, T. H. Zhuang, M. L. Feng and X. Y. Huang, *Chem. Eng. J.*, 2023, **460**, 141697.
53 S. Wang, P. Zhang, E. Ma, S. Chen, Z. Li, L. Yuan, J. Zu, L. Wang and W. Shi, *J. Hazard. Mater.*, 2024, **469**, 134079.
54 Z. Yuan, J. Q. Bi, W. L. Wang, X. N. Sun, L. Wang, J. J. Mao and F. S. Yang, *J. Appl. Biomater. Funct. Mater.*, 2021, **19**, 8.
55 L. Al-Attar, A. Dyer and R. Harjula, *J. Radioanal. Nucl. Chem.*, 2004, **260**, 199–203.
56 C. S. Griffith, V. Luca, J. Cochrane and J. V. Hanna, *Microporous Mesoporous Mater.*, 2008, **111**, 387–403.
57 M. A. Salam and R. C. Burk, *Appl. Surf. Sci.*, 2008, **255**, 1975–1981.
58 A. Dabrowski, P. Podkoscielny, Z. Hubicki and M. Barczak, *Chemosphere*, 2005, **58**, 1049–1070.
59 CCDC 2466544: Experimental Crystal Structure Determination, 2025, DOI: **10.5517/ccdc.csd.cc2nsmy1**.

